Structural Durability & Health Monitoring

Tech Science Press

https://doi.org/10.32604/sdhm.2026.075587

ARTICLE

Manufacturing of CFRP Plate Coupled with Large Range FBG

Mingxia Li[1,*], Haowei Xu[1], Ruiqi Li[1], Bo Song[2] and Wanxu Zhu[1,*]

[1]School of Civil Engineering, Guilin University of Technology, Guilin, China
[2]China Huaneng Zhasainuoer Coal Industry Co., Ltd., Hulunbuir, China

*Corresponding Authors: Mingxia Li. Email: limingxia172@163.com; Wanxu Zhu. Email: zhuwanxu@vip.163.com

Received: 04 November 2025; Accepted: 20 January 2026; Published: 18 May 2026

ABSTRACT: Conventional fiber Bragg grating (FBG) sensors used for tensile monitoring have a limited measurement range and therefore cannot cover the entire service stage of prestressed carbon-fiber-reinforced polymer (CFRP)–strengthened members. In this study, a smart CFRP plate is developed by embedding a wide-range FBG sensor in a prestressed CFRP plate. Based on strain-transfer theory for the grating region, an analytical expression for the average strain-transfer rate is derived and then used to inversely design the groove geometry and bonding parameters; the resulting groove size is 0.5 mm × 0.5 mm. During bonding, a tensile force of 0.3Pc is applied and maintained, where Pc denotes the theoretical ultimate tensile capacity of the plate, so that the embedded FBG remains in tension and potential slack at the bonded interfaces is eliminated. Three CFRP specimens (100 mm × 2 mm, width × thickness) are fabricated, and three rounds of cyclic calibration followed by monotonic tensile tests are conducted. In accordance with national standards for static performance, the sensitivity, hysteresis, linearity, repeatability, and root-sum-square (RSS) combined accuracy are quantified. The measured FBG strain sensitivity agrees well with the theoretical value of 1.21 pm/με. The measurable strain range reaches approximately 12,088.71 με, covering about 90% of the working interval up to the theoretical ultimate load of the member. The static performance indices are as follows: hysteresis ≤ 0.94%, linearity ≤ 0.57%, repeatability ≤ 2.82%, and overall accuracy ≤ 2.95%. The proposed approach markedly extends the monitoring range while maintaining accuracy, enabling continuous strain monitoring of CFRP-strengthened members from normal service to the pre-ultimate stage and meeting engineering requirements for both a wide range and high precision.

KEYWORDS: Whole-stage monitoring; intelligent CFRP plate; FBG sensor; tension test; stress strain

1 Introduction

Prestressed CFRP plates are extensively used to strengthen long-span flexural members (e.g., bridges) because of their high strength-to-weight and stiffness-to-weight ratios [1–3]. This strengthening method enhances load-carrying capacity, limits deflection, mitigates crack growth and, in some cases, helps to close existing cracks [4,5]. With broader deployment and longer service periods, durability assessment becomes increasingly challenging; consequently, life-cycle structural health monitoring (SHM) is gaining importance [6–8]. Traditional resistive and vibrating-wire sensors are vulnerable to temperature, moisture, and corrosion, making long-term, continuous, and highly reliable monitoring difficult [9,10]. In contrast, FBG sensors offer high precision, immunity to electromagnetic interference and multiplexing capability, and they can be embedded to measure internal stress/strain and detect early damage [11].

For through-life monitoring, FBGs can address the limitations of traditional sensors if their usable range spans all structural states. To broaden the usable range of FBGs, prior work explores material coupling

and packaging/installation refinements [12–14]. For material coupling, Li et al. developed a wide-range FBG strain sensor with a carbon fiber–based substrate adhered to its surface for measuring the strain and load of aircraft landing gear structures [15], thereby extending its measurement range to monitor multi-directional loads. Feng et al. combined an FBG sensor with austenitic stainless steel and niobium-based constant-elastic alloys to broaden the temperature measurement range [16]. Their results showed that the FBG sensor encapsulated with niobium-based alloy exhibited excellent temperature and strain sensing performance across a wide temperature range (30°C–250°C), which far exceeds the typical operating limit (below 175°C) of conventional electrical sensors used in oil and gas wells. Sanchez et al. developed an FBG-based sensor for torque and angle measurement by instrumenting the torsional spring of a series elastic actuator [17]. Their validation results indicate a torque measurement range of 15 N·m with an error on the order of 0.1 N·m [17]. These studies demonstrate that FBG sensors can be effectively integrated with different elastic structures and materials to meet application-specific sensing requirements. Regarding packaging and attachment, Kuang et al. summarized strain-sensing FBG implementations including fully pasted (adhesive-bonded) gratings, pre-stretched gratings with double-end fixation (mechanical fixation), and metallic-packaged gratings [18]. For metallic packaging, metallized FBGs can be welded (e.g., laser welding) to sensor components to improve durability in harsh environments and to avoid adhesive aging issues [18]. Zhou and Wang proposed an end-anchored intelligent CFRP plate assembly with built-in FBG sensors, enabling the CFRP plate to provide structural strengthening while simultaneously achieving full-range strain monitoring throughout the loading history [19]. Using the FBG-based monitoring data, they further evaluated the short-term prestress loss attributed to anchorage set and established the relationship between external load and CFRP strain at midspan for the strengthened member [19]. However, for adhesive-bonded FBG measurements, interfacial adhesive failure can introduce strain-transfer errors and lead to systematic deviations, thereby compromising measurement accuracy [20]. Furthermore, in practical reinforcement engineering, improper construction practices can easily damage or disable the FBGs [21]. Therefore, it is crucial to ensure measurement accuracy while minimizing on-site operational complexity. To enable real-time monitoring under extra-large strain conditions, Wang et al. developed a wide-range FBG strain sensor using a desensitization mechanism and demonstrated a measurement range up to 10,000 με with high linearity [22]. For surface-bonded optical fiber sensors, the measured strain may deviate from the substrate strain due to imperfect strain transfer through the adhesive and protective layers; therefore, the strain-transfer efficiency should be evaluated in sensor design and calibration [23]. However, studies have also shown that factors such as adhesive layer thickness and bonding material significantly affect the strain transfer ratio of embedded FBG sensors, introducing measurement errors during construction [24]. To overcome the limitations of external and adhesive packaging in terms of accuracy and manufacturability, Perry developed a fully metallic encapsulation scheme for FBG sensors [25], embedding the grating into a metal capillary tube via high-temperature induction brazing to prevent thermal damage. The sensor maintained stable strain detection even when the stress in prestressed steel strands reached approximately 1300 MPa (about 80% of their ultimate tensile strength), demonstrating excellent thermal stability and service life. Nevertheless, the process is complex, costly, and highly dependent on specialized technical expertise. Consequently, efficiently integrating FBG sensors into bridge reinforcement systems to achieve long-term, full-stage monitoring remains a major challenge.

To address this issue, this paper proposes a novel approach to fabricate a smart CFRP plate by coupling a large range FBG sensor within a prestressed CFRP plate. Based on the strain transfer theory of fiber Bragg gratings, the optimal groove dimensions in the middle section of the plate are determined. The FBG is embedded in the groove using an adhesive and further protected by a specialized encapsulation layer. Calibration and tensioning tests are conducted to evaluate the stress and strain measurement accuracy

and range of the smart CFRP plate, verifying its ability to meet the requirements of practical engineering applications. This method aims to achieve an integrated system for both reinforcement and monitoring, enabling full-stage structural health monitoring in bridge reinforcement projects.

Consequently, efficiently integrating FBG sensors into bridge-reinforcement systems to achieve long-term, full-stage monitoring remains challenging. Recent studies have also demonstrated the feasibility of integrating FBG sensors with CFRP reinforcement for monitoring prestressed concrete structures [26,27], which further motivates the development of a smart CFRP plate suitable for full-stage monitoring.

2 Design of Intelligent CFRP Plate

Because fiber Bragg gratings are made of brittle silica glass, they are vulnerable to damage under compression or bending. To improve the low survival rate after encapsulation of FBG sensors embedded in CFRP plates, a groove-embedded encapsulation method is adopted. A longitudinal groove is machined along the plate midline; the FBG is placed in the recess, bonded with a structural adhesive, and then protected by an over-encapsulation layer. In addition, a fixed end-clamping plate (pressure strip) is used to protect the FBG terminations and improve the stability of strain transfer. Fig. 1 presents the structural schematic of the FBG-integrated smart CFRP plate, and Fig. 2 shows a fabricated specimen.

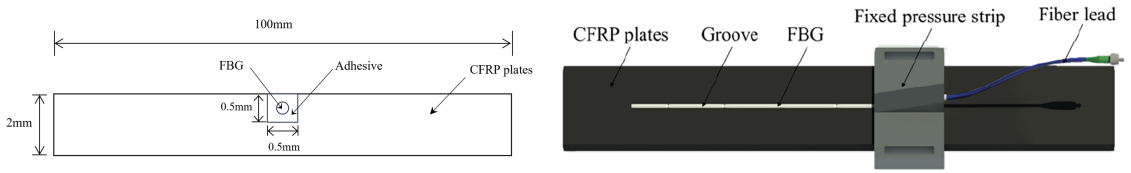

(**a**) Schematic diagram of cross section (**b**) Three-dimensional diagram

Figure 1: Schematic diagram of FBG intelligent CFRP plate.

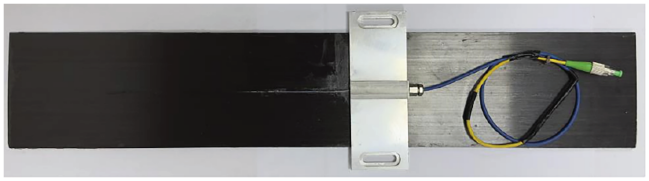

Figure 2: Photograph of the FBG-integrated smart CFRP plate.

2.1 Strain Sensing Principle of FBG Sensors

The basic strain-sensing principle of an FBG is that when light propagates through a phase grating with a specific grating period recorded in the fiber core, the light that satisfies the Bragg condition is reflected back. The relationship between the effective refractive index, the grating period, and the central wavelength is given by Eq. (1):

$$\lambda_B = 2n_{eff}\Lambda \tag{1}$$

where λ_B is the Bragg (central) wavelength, n_{eff} is the effective refractive index of the fiber core and Λ is the grating period.

When external deformation is transmitted to the grating region, the grating period changes and the photoelastic effect leads to variations in the effective refractive index. Consequently, the central wavelength shifts. Neglecting temperature effects, the linear relationship between the axial strain ε and the central-wavelength variation $\Delta\lambda$ can be expressed by Eq. (2):

$$\Delta\lambda = \left\{1 - \frac{n_{eff}^2}{2}\left[P_{12} - \mu\left(P_{11} + P_{12}\right)\right]\right\} \cdot \lambda_B \cdot \varepsilon = \lambda_B\left(1 - P_e\right)\varepsilon = K_\varepsilon \varepsilon \tag{2}$$

where $\Delta\lambda$ is the Bragg wavelength shift of the FBG, λ_B is the initial Bragg wavelength, ε is the axial strain, μ is Poisson's ratio, p_{11}, p_{12} are the strain-optic coefficients, P_e is the effective photoelastic coefficient, and K_ε is the strain sensitivity coefficient of the FBG.

For the elastic-optical coefficient P_e is 0.22 of the fiber made of ordinary quartz, it can be seen from Eq. (2) that the strain sensitivity coefficient K_ε of fiber grating with center wavelength of 1534~1560 nm is 1.21 pm/με.

2.2 Strain Transfer Theory of FBG Sensors in Groove of CFRP Plate

To reliably relate the strain recorded by the FBG embedded in the groove to the actual strain of the CFRP plate, the strain-transfer process from the substrate to the fiber is modeled and corrected. This enables quantitative design of the groove geometry and bonded length. The coating and adhesive layers are the principal structural layers governing strain transfer to the fiber core (Figs. 3 and 4 [28]). Because shear deformation occurs in both the coating and the external adhesive, the strain indicated by the FBG must be corrected to recover the actual structural strain. The model is based on the following assumptions: (1) All constituents are linear elastic; the CFRP plate is subjected to a uniform axial tensile stress, which is transmitted to the fiber core through shear deformation of the adhesive and coating layers, while the fiber undergoes only axial deformation; (2) No interfacial slip occurs between the CFRP plate, adhesive, coating, and fiber core; (3) Shear deformation in structural layers other than the adhesive and coating is neglected; (4) The fiber core, coating, adhesive, and CFRP plate exhibit comparable axial-strain gradients.

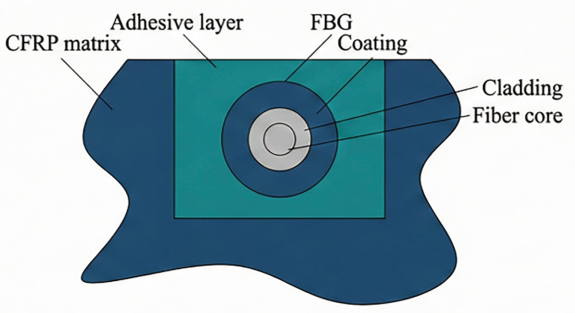

Figure 3: Cross section of intelligent CFRP plate (Redrawn from Ref. [28]).

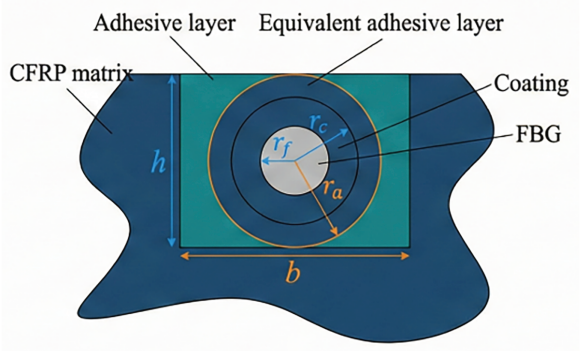

Figure 4: Simplified schematic diagram of CFRP plate (Redrawn from Ref. [28]).

To model strain transfer to the optical fiber, the silica (SiO_2) fiber and its protective coating, which have nearly the same shear modulus, are treated as a single core and represented as a concentric cylinder. The groove in the carbon-fiber plate is taken as a rectangle of width b and depth h; for analytical convenience, an area-equivalent circular section of diameter h is used. Taking the grating midpoint as the plane of symmetry, deformation compatibility is imposed across the layers, and the relationship between the strain in the embedded FBG and the strain in the substrate is derived. This model provides a quantitative mapping from the average strain over the grating length to the actual substrate strain. The mapping guides the choice of groove dimensions and bonded length and supports calibration and correction of subsequent measurements.

As shown in Fig. 5 [26], the force analysis of the fiber core micro-element is carried out:

$$\pi r_f^2 d\sigma_f(x) + 2\pi r_f \tau_{cf}\left(x, r_f\right) dx = 0 \tag{3}$$

where r_f is the distance from the outer surface of the fiber core layer to the fiber axis, and σ_f is the normal stress of the fiber core layer, and τ_{cf} is the shear stress of the coating layer and the fiber core layer.

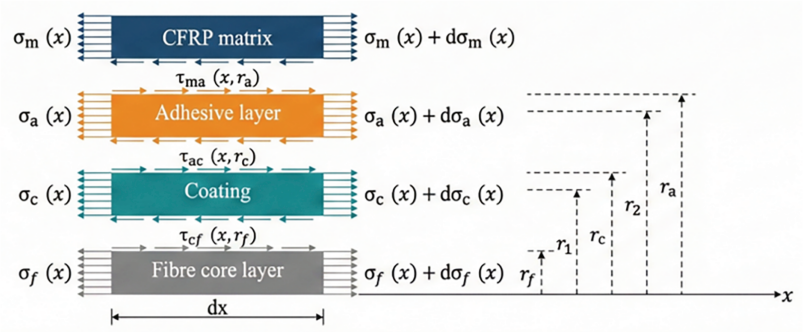

Figure 5: Force analysis of micro element (Redrawn from Ref. [26]).

As shown in Fig. 5 [26], the force analysis of the coating micro-element can be expressed as follows:

$$\pi\left(r_1^2 - r_f^2\right) d\sigma_c(x) + 2\pi r_1 \tau_c(x, r_1) dx = 2\pi r_f \tau_{cf}\left(x, r_f\right) dx \tag{4}$$

where r_1 is the distance from any point in the coating layer to the axis of the fiber core layer, and σ_c is the normal stress of the coating layer, and τ_c is the shear stress in the coating layer.

Substituting Eq. (3) into (4):

$$\tau_c(x, r_1) = -\frac{r_f^2}{2r_1}\frac{d\sigma_f(x)}{dx} - \frac{r_1^2 - r_f^2}{2r_1}\frac{d\sigma_c(x)}{dx} \tag{5}$$

As shown in Fig. 5 [26], the stress analysis of the bonding layer micro-element can be performed as follows:

$$\pi\left(r_2^2 - r_c^2\right)d\sigma_a(x) + 2\pi r_2\tau_a(x, r_2)\,dx = 2\pi r_c\tau_{ac}(x, r_c)\,dx \tag{6}$$

where r_2 is the distance from any point in the bonding layer to the axis of the fiber core layer, and σ_a is the normal stress of the bonding layer, and τ_a is the shear stress in the bonding layer.

Substituting Eq. (5) into (6), we can obtain as follows:

$$\tau_c(x, r_2) = -\frac{r_f^2}{2r_2}\frac{d\sigma_f(x)}{dx} - \frac{r_c^2 - r_f^2}{2r_2}\frac{d\sigma_c(x)}{dx} - \frac{r_2^2 - r_c^2}{2r_2}\frac{d\sigma_a(x)}{dx} \tag{7}$$

According to Hooke's law, the normal stress of fiber core, coating layer and bonding layer can be given as follows:

$$\sigma_f(x) = E_f\varepsilon_f(x) \tag{8}$$

$$\sigma_c(x) = E_c\varepsilon_c(x) \tag{9}$$

$$\sigma_a(x) = E_a\varepsilon_a(x) \tag{10}$$

where E_f, E_c and E_a are the elastic modulus of the fiber core, the coating layer and the bonding layer, respectively; $\varepsilon_f(x)$, $\varepsilon_c(x)$ and $\varepsilon_a(x)$ are the axial strain of the fiber core, the coating layer and the bonding layer, respectively.

With the Poisson effect neglected, substitution of Eqs. (8) and (9) into Eq. (5) yields the shear stress in the coating layer:

$$\begin{aligned}\tau_c(x, r_1) &= -\frac{r_f^2}{2r_1}E_f\frac{d\varepsilon_f(x)}{dx} - \frac{{r_1}^2 - r_f^2}{2r_1}E_c\frac{d\varepsilon_c(x)}{dx} \\ &= -\frac{E_f r_f^2}{2r_1}\left[\frac{d\varepsilon_f(x)}{dx} + \frac{{r_1}^2 - r_f^2}{r_f^2}\frac{E_c}{E_f}\frac{d\varepsilon_c(x)}{dx}\right]\end{aligned} \tag{11}$$

Neglecting the Poisson effect, substitution of Eqs. (8)–(10) into Eq. (7) yields the shear stress in the bonding layer:

$$\begin{aligned}\tau_a(x, r_2) &= -\frac{r_f^2}{2r_2}E_f\frac{d\varepsilon_f(x)}{dx} - \frac{{r_c}^2 - r_f^2}{2r_2}E_c\frac{d\varepsilon_c(x)}{dx} - \frac{{r_2}^2 - r_c^2}{2r_2}E_a\frac{d\varepsilon_a(x)}{dx} \\ &= -\frac{E_f r_f^2}{2r_2}\left[\frac{d\varepsilon_f(x)}{dx} + \frac{{r_c}^2 - r_f^2}{r_f^2}\frac{E_c}{E_f}\frac{d\varepsilon_c(x)}{dx} + \frac{{r_2}^2 - r_c^2}{r_f^2}\frac{E_a}{E_f}\frac{d\varepsilon_a(x)}{dx}\right]\end{aligned} \tag{12}$$

According to the assumption (4) that the fiber grating core layer and the cementation layer deform synchronously, the strain gradients of the two are similar, and it can be considered as:

$$\frac{d\varepsilon_f(x)}{dx} \cong \frac{d\varepsilon_c(x)}{dx} \cong \frac{d\varepsilon_a(x)}{dx} \tag{13}$$

Since the fiber grating core layer has a much larger modulus of elasticity than the coating and bonding layers, it can be concluded as follows:

$$\frac{E_a}{E_f} \cong \frac{E_c}{E_f} = 0 \tag{14}$$

Substituting Eqs. (13) and (14) into (11), the shear stress of the coating layer can be simplified as:

$$\tau_c(x, r_1) = -\frac{E_f r_f^2}{2r_1}\frac{d\varepsilon_f(x)}{dx} \tag{15}$$

Substituting Eqs. (13) and (14) into (12), the shear stress of the bonding layer can be simplified by following:

$$\tau_a(x, r_2) = -\frac{E_f r_f^2}{2r_2}\frac{d\varepsilon_f(x)}{dx} \tag{16}$$

According to the deformation relationship of each layer in Fig. 6 and Assumption (2), the deformation relationship of each structural layer can be obtained by deformation coordination as follows:

$$u_m(x) = \Delta_a(x) + \Delta_c(x) + u_f(x) \tag{17}$$

where u_m and u_f are the axial displacement of the carbon fiber matrix layer and the fiber core layer, respectively; $\Delta_a(x)$ and $\Delta_c(x)$ are the shear displacement of the bonding layer and the coating layer, respectively.

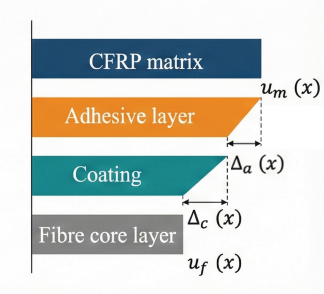

Figure 6: Deformation relationship of each layer.

Based on Hooke's law, the shear strain of the bonding and coating layers can be given as follows:

$$\gamma_c(x) = \frac{\tau_c(x, r_1)}{G_c} \tag{18}$$

$$\gamma_a(x) = \frac{\tau_a(x, r_2)}{G_a} \tag{19}$$

where γ_c and γ_a are the shear strain of the bonding layer and the coating layer, respectively; G_c and G_a are the shear modulus of the bonding layer and the coating layer, respectively.

Substitution of Eq. (15) into Eq. (18) yields the shear displacement in the coating layer:

$$\Delta_c(x) = \int_{r_f}^{r_c} \frac{\tau_c(x, r_1)}{G_c} dr_1 = -\frac{r_f^2 E_f}{2G_c} \ln \frac{r_c}{r_f} \frac{d\varepsilon_f(x)}{dx} \tag{20}$$

Substitution of Eq. (16) into (19) yields the shear displacement in the bonding layer:

$$\Delta_a(x) = \int_{r_c}^{r_a} \frac{\tau_a(x, r_2)}{G_a} dr = -\frac{r_f^2 E_f}{2G_a} \ln \frac{r_a}{r_c} \frac{d\varepsilon_f(x)}{dx} \tag{21}$$

Substituting Eq. (21) into (17) and deriving x on both sides of the equation gives:

$$\varepsilon_m(x) = \varepsilon_f(x) - \left[\frac{r_f^2 E_f}{2G_c} \ln \frac{r_c}{r_f} + \frac{r_f^2 E_f}{2G_a} \ln \frac{r_a}{r_c} \right] \frac{d\varepsilon_f^2(x)}{dx^2} \tag{22}$$

Keeping $k^2 = 1 \Big/ \left[\frac{r_f^2 E_f}{2G_c} \ln \frac{r_c}{r_f} + \frac{r_f^2 E_f}{2G_a} \ln \frac{r_a}{r_c} \right]$, and according to the assumption (1), the strain of carbon fiber plate is a fixed value ε_c, then the Eq. (22) can be simplified as follows:

$$\frac{d^2\varepsilon_f(x)}{dx^2} - k^2 \varepsilon_f(x) = -k^2 \varepsilon_m \tag{23}$$

The general solution of Eq. (23) can be expressed as:

$$\varepsilon_f(x) = C_1 e^{kx} + C_2 e^{-kx} + \varepsilon_m \tag{24}$$

According to the structure, the strain of the fiber core layer at the end and tail of the bond is 0, it means that $\varepsilon_f(L) = \varepsilon_f(-L) = 0$, which can be obtained as follows:

$$C_1 = C_2 = -\frac{\varepsilon_c}{2ch(kL)} \tag{25}$$

$$\varepsilon_f(x) = \varepsilon_m \left[1 - \frac{ch(kx)}{ch(kL)} \right] \tag{26}$$

where $\varepsilon_f(x)$ is the axial strain in the FBG core, ε_m denotes the uniform axial strain of the CFRP plate (substrate), and the symbols ε_f and ε_m are hereafter consistently used for fiber and matrix strains, respectively. Here, k is the shear-lag parameter determined by the geometry and the shear moduli of the adhesive and coating layers.

The measured value of FBG strain sensor is the average strain value within the grating length of the fiber grating region. The grating is arranged in the middle section of the bonding section with high strain transfer rate and uniform distribution of the sensor. Assuming that the grating length is $2L_f$, according to the symmetry calculation, the average strain of the grating in this area can be expressed as:

$$\overline{\varepsilon_f}(L_f) = \frac{\int_0^{L_f} \varepsilon_f(x)\, dx}{L_f} \tag{27}$$

According to Eq. (27), the average strain-transfer rate of the grating is:

$$\alpha\left(k, L_f\right)=\frac{\overline{\varepsilon_f}\left(L_f\right)}{\varepsilon_m}=1-\frac{sh\left(kL_f\right)}{kL_f ch\left(kL\right)}, k^2=1\Big/\left[\frac{r_f^2 E_f}{2G_c}\ln\frac{r_c}{r_f}+\frac{r_f^2 E_f}{2G_a}\ln\frac{r_a}{r_c}\right] \tag{28}$$

where $\alpha\left(k, L_f\right)$ is the average strain-transfer coefficient of the grating, is the uniform axial strain of the CFRP plate, and L is the half-length of the bonded region so that the total bonded length is $2L$. The symbols *sh* and *ch* denote the hyperbolic sine and hyperbolic cosine functions. In addition, r_f is the radius of the fiber core, r_c is the outer radius of the coating layer, and r_d is the outer radius at the adhesive boundary. E_f is the Young's modulus of the fiber core, G_c is the shear modulus of the coating layer, and G_a is the shear modulus of the adhesive layer. The term ln denotes the natural logarithm.

2.3 Groove Theoretical Design of Intelligent CFRP Plate

To prevent the FBG from being forced out of the groove when the CFRP plate is in tension, the adhesive-layer thickness must be smaller than the groove depth, and the groove cross-section must not significantly weaken the plate. Adequate groove depth and width also increase the contact area and transverse restraint, reducing slip between the adhesive and the plate. These considerations define the sizing constraints. The encapsulation system consists of an epoxy adhesive (shear modulus G_a = 379 MPa), an acrylate coating (G_c = 338 MPa), and a silica fiber core with modulus E_f = 72 GPa and radii r_f = 0.125 mm and r_c = 0.250 mm. Using Eq. (28), the influences of adhesive-layer thickness and bonded length L on the average strain-transfer ratio $\alpha \approx 1$ within the grating region are evaluated, as shown in Fig. 7. Thinner adhesive layers and longer bonded lengths increase α. The coefficient rises rapidly for $L < 17$ mm and approaches a plateau for $L > 30$ mm, indicating that α is more sensitive to L than to adhesive-layer thickness. Because the adhesive thickness determines the groove depth and hence affects the structural capacity of the plate, a target of $\alpha \approx 1$ is adopted. First, the minimum safe adhesive thickness not exceeding the groove depth is selected, and then L is chosen in the plateau region so that α is as close to unity as possible.

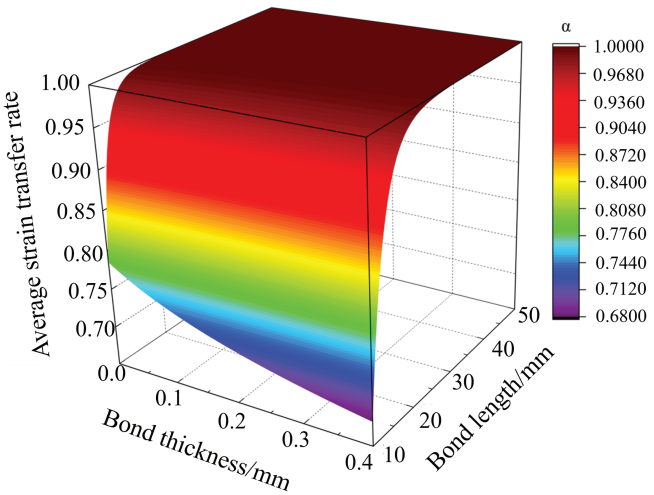

Figure 7: Effect of bond thickness and bond length on average strain transfer rate.

Balancing these factors, the groove depth and width are set to 0.5 mm, the adhesive thickness to 0.4 mm (satisfying the requirement "adhesive thickness < groove depth"), and the bonded length to 40 mm, which lies in the plateau region. The grating length is 10 mm. With these values, Eq. (28) gives a strain-transfer

coefficient very close to unity ($\alpha > 0.99$). Therefore, the correction from the measured FBG strain to the substrate strain is negligible under the present configuration, and the substrate strain can be approximated as given by Eq. (29).

$$\varepsilon_m = \frac{\overline{\varepsilon_f}\left(L_f\right)}{\alpha} \approx \overline{\varepsilon_f}\left(L_f\right) \tag{29}$$

Finally, the mechanical consequence of introducing the groove is evaluated. Because the groove locally reduces the cross-sectional area of the CFRP plate, its influence on tensile strength must also be considered. The groove dimensions (0.5 mm × 0.5 mm) remove approximately 0.25 mm^2 of material from a gross cross-section of 100 mm × 2 mm = 200 mm^2, corresponding to a nominal area reduction of only about 0.125%. Therefore, the change in average tensile capacity is expected to be negligible. The groove edges were machined with smooth corners to avoid sharp notches and to limit stress concentration. In the tensile tests, all three smart CFRP plates failed in the anchorage zone adjacent to the grips, and no cracking or debonding was observed to initiate from the grooved region prior to rupture, indicating that the grooving process did not trigger premature failure. Taken together, these observations suggest that the present groove configuration has only a minor effect on the ultimate tensile strength of the CFRP plate, although more detailed numerical analysis and comparative testing on grooved and ungrooved plates will be considered in future work.

3 Experimental Investigation on Large-Scale Intelligent CFRP Plate

The specimens were 2400 MPa-grade CFRP plates with dimensions 100 mm × 2 mm, where the dimensions are given as width × thickness. The FBG had a 3-dB bandwidth of 0.21 nm and a reflectivity of 0.93. Wavelengths were measured using an Agilent 86142B optical spectrum analyzer with a range of 1525–1570 nm, a sampling rate of 1 Hz, wavelength accuracy of 2.5 pm, and a resolution of 1 pm.

A groove 0.5 mm deep was machined along the midline of each plate, as shown in Fig. 8. Each CFRP plate was mounted in a tensile loading frame and preloaded to 0.3Pc, where Pc denotes the theoretical ultimate tensile capacity of the plate. This preload level was selected as a compromise between sensing and structural requirements: it is sufficiently high to maintain the embedded FBG in tension throughout the expected service life and to eliminate any initial slack in the groove–adhesive–fiber system during curing, while remaining well below the ultimate capacity to minimize the risk of damaging the CFRP plate or its anchorage during fabrication. Once the target preload was reached, the FBG was bonded into the groove with epoxy adhesive, symmetrically about the grating midpoint, with 20 mm bonded on each side. The preload was maintained until the epoxy fully cured, resulting in a smart CFRP plate with an embedded FBG sensor. Three plates, labeled A, B, and C, were fabricated and subsequently tested sequentially for calibration and tensile performance.

3.1 Calibration Test of Intelligent CFRP Plates

Each CFRP plate instrumented with an FBG sensor underwent three calibration cycles of loading-unloading. The procedure was as follows: first, preload to 0.1Pc and hold for 5 min to verify proper FBG operation; then, reduce the load to 5 kN and, after the load cell and FBG demodulator readings stabilize, record the initial center wavelength. Next, apply stepwise loading in increments of 0.05Pc at a rate not exceeding 100 MPa/min; after each step, wait for stabilization and record the force and the center wavelength. Continue loading to 0.7Pc, record as required, hold for 5 min, and then unload in 0.05Pc steps while

recording stabilized readings at each level. Repeat steps 2 through 5 three times for each specimen to complete the calibration.

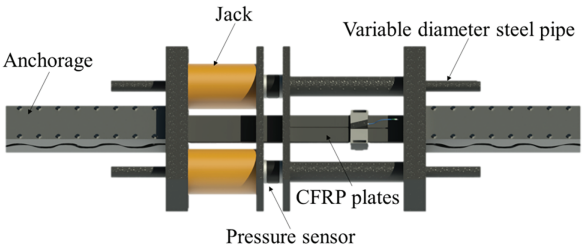

Figure 8: Picture of experimental set up of intelligent CFRP plate.

The collected data were used to plot load–wavelength curves with load on the *x*-axis and the grating's center wavelength on the *y*-axis, as shown in Fig. 9 [29]. The center wavelength increased linearly with load, and the three cycles nearly overlapped, demonstrating excellent repeatability and agreement with theory.

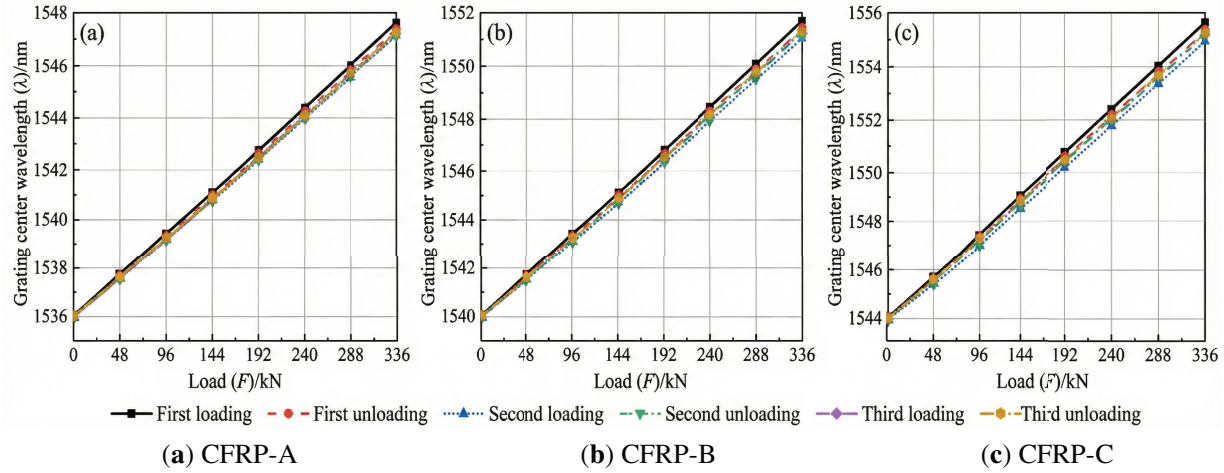

Figure 9: Load-wavelength curve in calibration test of CFRP plates (Redrawn from Ref. [29]).

3.2 Tensile Test of Intelligent CFRP Plates

After the cyclic loading–unloading test, a quasi-static tensile test was conducted. Loading was applied in increments of $0.05P_c$ up to $0.7P_c$, followed by finer increments of $0.025\ P_c$. After each step, once the load-cell and FBG demodulator readings stabilized, the force, center wavelength, and reference strain were recorded. Loading continued to failure of the CFRP plate.

In all three tests, the CFRP plates failed in the anchorage zone adjacent to the grips, and no visible cracking or debonding was observed around the grooved FBG region prior to rupture. The embedded FBG sensors exhibited stable, monotonic wavelength shifts throughout loading and remained functional until just before plate fracture, with no premature dropouts or abnormal jumps in the signal. In particular, all three groove-embedded FBG sensors survived the entire fabrication, calibration, and tensile-testing programme, yielding a 100% post-encapsulation survival rate in this small sample. These observations indicate that the groove-embedded configuration does not induce or promote premature failure of either the plate or the sensor.

The test followed the encapsulation and calibration conditions established previously, for which the strain-transfer coefficient satisfies $\alpha \approx 1$. The primary objective was to determine the FBG strain sensitivity. A linear regression was fitted with the midspan strain from the foil gauge as the independent variable and the change in FBG center wavelength as the dependent variable, as shown in Fig. 10 [27]. The slope of this fit gives the wavelength–strain sensitivity. The strain interval over which the linear relation satisfies the specified error limit was taken as the monitoring range and was verified to lie within the demodulator's spectral measurement window.

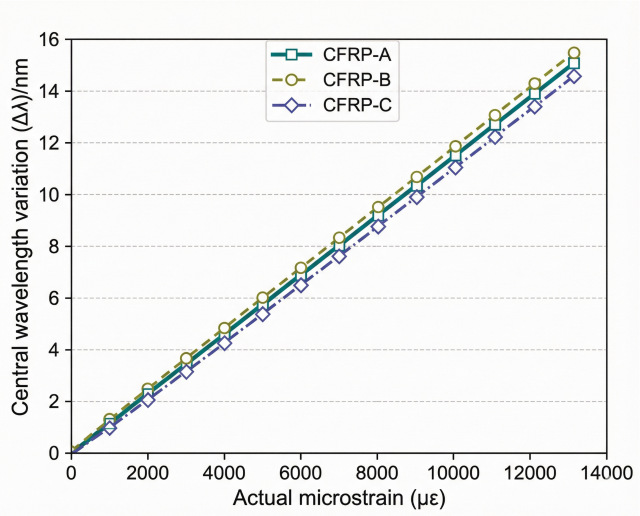

Figure 10: The relationship between wavelength variation of FBG sensors and strain of CFRP plates (Adapted from Ref. [27]).

4 Performance Analysis of Large Range Intelligent CFRP Plates

Three CFRP plates instrumented with embedded FBG strain sensors were calibrated, and the static performance of the sensors was quantified in accordance with the national standard GB/T 18459–2001, Calculation Methods for Main Static Performance Indicators of Sensors. Here, "static" refers to the steady relationship between input and output when the plate strain is constant or varies only slowly. The evaluated metrics are strain sensitivity, hysteresis, linearity, repeatability, and total accuracy.

Three CFRP plates instrumented with embedded FBG strain sensors are calibrated, and the static performance of the sensors is quantified in accordance with the national standard GB/T 18459–2001, Calculation Methods for Main Static Performance Indicators of Sensors. Here, "static" refers to the steady relationship between input and output when the plate strain is constant or varies only slowly. The evaluated metrics are strain sensitivity, hysteresis, linearity, repeatability, and total accuracy.

4.1 Strain Sensitivity

During static tensile testing, the strain sensitivity of the grating is defined as the FBG center-wavelength shift to the substrate strain. As shown in Fig. 10.

According to Fig. 10 and Table 1, it can be seen that the linearity of the experimental data is excellent, the strain sensitivity of the CFRP plate coupled with the fiber grating is not less than 1.21 pm/με, and the maximum strain monitored by the CFRP plate reaches 12104.84 με.

Table 1: Strain sensitivity of intelligent CFRP plates.

Specimen	Relationship between Center Wavelength Variation and Strain of Strain Sensor	Linear Correlation	Monitoring Range
CFRP-A	$\Delta\lambda = 0.00121\ \mu\varepsilon + 0.05076$	99.981%	12102.15 με
CFRP-B	$\Delta\lambda = 0.00122\ \mu\varepsilon + 0.02452$	99.993%	12104.84 με
CFRP-C	$\Delta\lambda = 0.00122\ \mu\varepsilon + 0.04878$	99.975%	12088.71 με

The experimentally obtained FBG strain sensitivity is generally consistent with the theoretical calculation result of 1.21 pm/με, though sensitivity varies among some gratings. The primary reasons for this discrepancy are:

(1) Material property variations in the epoxy adhesive layer: The actual epoxy resin used deviates from the ideal parameters in the theoretical model, leading to inconsistent strain transmission efficiency and consequently affecting sensor sensitivity.
(2) Geometric simplification errors: Theoretical modeling typically treats FBG sensors as circular cross-sections, whereas actual grooves have rectangular cross-sections. This structural discrepancy alters the strain transmission path.
(3) Manual assembly errors: During the embedding of the fiber Bragg grating into the CFRP plate groove, manual operations cannot fully guarantee axial parallelism between the FBG sensor and the CFRP plate. This results in a deviation between the strain perceived by the FBG and the actual strain.

4.2 Hysteresis

Hysteresis refers to the mismatch between the loading and unloading center-wavelength shift curves of the grating during loading and unloading of the measured substrate. Analysis of the calibration test data for the three CFRP plates in Fig. 9 yields the arithmetic mean of the center wavelength changes during loading and unloading, along with their respective differences. The results for plates A, B, and C are shown in Tables 2–4, respectively.

Table 2: The center wavelength variation and deviation value of A grating during loading and unloading.

Load/kN	Average Value when Loading/nm	Average Value when Unloading/nm	Deviation Value/nm
5	0.0000	0.0000	0.0000
24	0.7342	0.5988	0.1353
48	1.4113	1.4287	−0.0175
72	2.1968	2.2641	−0.0672
96	3.0202	2.9638	0.0564
120	3.7568	3.8276	−0.0708
144	4.5906	4.5322	0.0584
168	5.3991	5.3459	0.0532
192	6.2168	6.1762	0.0406
216	6.8819	6.9230	−0.0411
240	7.7126	7.7174	−0.0048
264	8.4412	8.4412	0.0000

(Continued)

Table 2 (continued)

Load/kN	Average Value when Loading/nm	Average Value when Unloading/nm	Deviation Value/nm
288	9.2933	9.2551	0.0382
312	10.0228	9.9966	0.0263
336	10.7945	10.8527	−0.0582

Table 3: The center wavelength variation and deviation value of B grating during loading and unloading.

Load/kN	Average Value when Loading/nm	Average Value when Unloading/nm	Deviation Value/nm
5	0.0000	0.0000	0.0000
24	0.6773	0.6108	0.0665
48	1.3522	1.4837	−0.1315
72	2.2285	2.2683	−0.0399
96	3.0232	3.0480	−0.0248
120	3.7786	3.8309	−0.0523
144	4.5710	4.6561	−0.0852
168	5.3425	5.3742	−0.0317
192	6.2299	6.1967	0.0332
216	6.9185	6.9240	−0.0055
240	7.6679	7.6983	−0.0304
264	8.5561	8.5413	0.0148
288	9.3362	9.3347	0.0015
312	10.1563	10.0983	0.0580
336	10.8861	10.9161	−0.0300

Table 4: The center wavelength variation and deviation value of C grating during loading and unloading.

Load/kN	Average Value when Loading/nm	Average Value when Unloading/nm	Deviation Value/nm
5	0.0000	0.0000	0.0000
24	0.7657	0.6667	0.0990
48	1.4682	1.4303	0.0379
72	2.3043	2.2939	0.0104
96	3.0246	3.0008	0.0237
120	3.8408	3.8814	−0.0405
144	4.6658	4.5993	0.0665
168	5.3671	5.4520	−0.0849
192	6.2826	6.1926	0.0900
216	6.9750	6.9791	−0.0041
240	7.8121	7.7877	0.0244

(Continued)

Table 4 (continued)

Load/kN	Average Value when Loading/nm	Average Value when Unloading/nm	Deviation Value/nm
264	8.5355	8.5706	−0.0351
288	9.4045	9.4143	−0.0098
312	10.1241	10.1807	−0.0565
336	10.9656	10.8754	0.0902

The hysteresis of the smart carbon fiber plate is defined as the maximum deviation between the average values of the central wavelength changes recorded by the strain sensor during three loading and unloading cycles. The calculation formula is shown in Eq. (30):

$$\xi_H = \frac{\Delta\lambda_{H,\max}}{(\Delta\lambda)_{FS}} \times 100\% \tag{30}$$

where $\Delta\lambda_{H,\max}$ is the maximum deviation between the mean wavelength shifts obtained from the loading and unloading curves (i.e., the maximum difference between the averaged loading and unloading responses), and $\Delta\lambda_{FS}$ is the full-scale wavelength shift over the calibration range. In this study, $\Delta\lambda_{FS}$ is taken as the experimentally calibrated output span, defined as $\Delta\lambda_{FS} = \lambda_{\max} - \lambda_{\min}$ within the calibration interval (from 5 kN to 0.7Pc). According to Tables 2–4, the maximum deviation of the center wavelength of the grating of each specimen is 0.1353 nm, 0.1315 nm and 0.0990 nm, respectively. The hysteresis of the three gratings obtained by substitution Eq. (30) is $\xi_{H,A} = 0.94\%$, $\xi_{H,B} = 0.90\%$ and $\xi_{H,C} = 0.68\%$, respectively.

4.3 Linearity

"Linearity, typically quantified by non-linearity error, represents the degree to which a sensor's output conforms to a linear relationship. It is defined as the maximum deviation of the actual calibration curve from the ideal best-fit line, expressed as a percentage of the full-scale output". According to the test data of Fig. 9, the index of the coincidence degree between the calibration curve of the arithmetic mean of the load and the grating wavelength change and the fitting line of the strain sensor under the three loading and unloading cyclic loads can be calculated using Eq. (31):

$$\xi_L = \frac{\Delta\lambda_{L,\max}}{(\Delta\lambda)_{FS}} \times 100\% \tag{31}$$

where $\Delta\lambda_{L,\max}$ is the maximum deviation of the grating center wavelength obtained under the same load level among repeated calibration cycles (for loading or unloading, respectively), and $\Delta\lambda_{FS}$ is the full-scale wavelength shift defined as $\Delta\lambda_{FS} = \lambda_{\max} - \lambda_{\min}$ within the experimental calibration interval (5 kN to 0.7Pc). The least squares method is used to linearly fit the data in Tables 2–4, and finally the results of Fig. 11 are obtained.

From the fitting line equation in Fig. 11, the fitting value of the variation of the grating center wavelength value of the grating on the three specimens during loading and unloading can be obtained. Combined with the arithmetic mean of the variation of the grating center wavelength value in Tables 2–4, the difference between the two can be obtained, as shown in Tables 5–7.

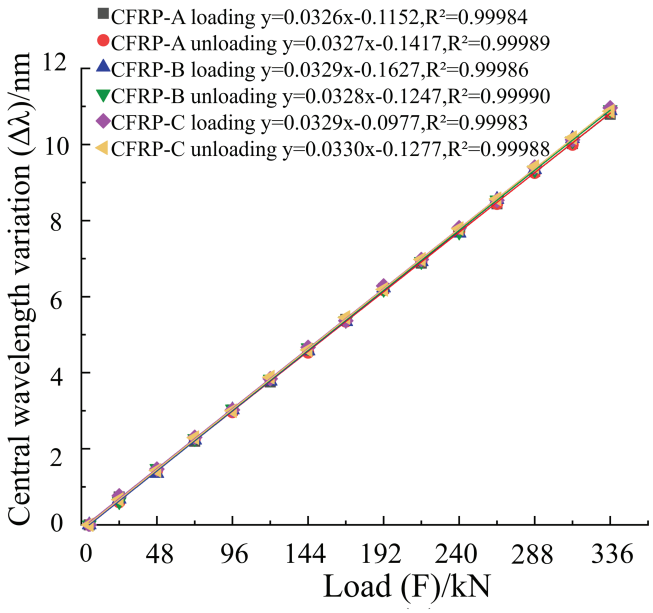

Figure 11: The relationship between the arithmetical mean variation of the central wavelength and the load.

Table 5: The difference between the average value of the wavelength variation of A grating and the fitting value during loading and unloading.

Load/kN	Fitting Values/nm		The Difference with the Average Value/nm	
	Load	Unload	Load	Unload
5	0.0476	0.0215	−0.0476	−0.0215
24	0.6661	0.6419	0.0681	−0.0430
48	1.4473	1.4255	−0.0360	0.0033
72	2.2285	2.2091	−0.0316	0.0550
96	3.0097	2.9927	0.0105	−0.0289
120	3.7909	3.7763	−0.0340	0.0514
144	4.5721	4.5599	0.0186	−0.0277
168	5.3533	5.3435	0.0458	0.0024
192	6.1345	6.1271	0.0823	0.0491
216	6.9157	6.9107	−0.0337	0.0124
240	7.6969	7.6943	0.0158	0.0232
264	8.4781	8.4779	−0.0369	−0.0367
288	9.2593	9.2615	0.0340	−0.0063
312	10.0405	10.0451	−0.0176	−0.0485
336	10.8217	10.8287	−0.0272	0.0240

Table 6: The difference between the average value of the wavelength variation of B grating and the fitting value during loading and unloading.

Load/kN	Fitting Values/nm		The Difference with the Average Value/nm	
	Load	Unload	Load	Unload
5	0.0020	0.0393	−0.0020	−0.0393
24	0.6279	0.6627	0.0494	−0.0519
48	1.4185	1.4502	−0.0662	0.0335
72	2.2090	2.2376	0.0195	0.0308
96	2.9996	3.0250	0.0237	0.0230
120	3.7901	3.8125	−0.0116	0.0184
144	4.5807	4.5999	−0.0097	0.0562
168	5.3713	5.3874	−0.0288	−0.0132
192	6.1618	6.1748	0.0681	0.0219
216	6.9524	6.9622	−0.0338	−0.0382
240	7.7429	7.7497	−0.0750	−0.0513
264	8.5335	8.5371	0.0226	0.0041
288	9.3241	9.3246	0.0121	0.0101
312	10.1146	10.1120	0.0417	−0.0137
336	10.9052	10.8994	−0.0190	0.0167

Table 7: The difference between the average value of the wavelength variation of C grating and the fitting value during loading and unloading.

Load/kN	Fitting Values/nm		The Difference with the Average Value/nm	
	Load	Unload	Load	Unload
5	0.0666	0.0372	−0.0666	−0.0372
24	0.6911	0.6636	0.0745	0.0031
48	1.4800	1.4549	−0.0119	−0.0246
72	2.2689	2.2462	0.0354	0.0477
96	3.0578	3.0374	−0.0332	−0.0366
120	3.8467	3.8287	−0.0058	0.0526
144	4.6355	4.6200	0.0303	−0.0206
168	5.4244	5.4113	−0.0573	0.0408
192	6.2133	6.2026	0.0693	−0.0099
216	7.0022	6.9938	−0.0272	−0.0147
240	7.7911	7.7851	0.0210	0.0026
264	8.5799	8.5764	−0.0445	−0.0058
288	9.3688	9.3677	0.0357	0.0466
312	10.1577	10.1590	−0.0336	0.0217
336	10.9466	10.9502	0.0190	−0.0748

From Tables 5–7, the maximum difference between the average value and the fitted value of the grating center wavelength variation of the three specimens can be obtained: for CFRP-A, it is 0.0823 nm when loaded

and 0.0550 nm when unloaded. For the specimen CFRP-B, the loading is 0.0750 nm, and the unloading is 0.0562 nm; for the specimen CFRP-C, the loading is 0.0745 nm and the unloading is 0.0748 nm.

According to the Eq. (30), the linearity of intelligent CFRP plates can be calculated as: for the specimen CFRP-A, when loaded $\xi_{L,Al}$ = 0.57%, when unloaded $\xi_{L,Au}$ = 0.38%; for the specimen CFRP-B, when loaded $\xi_{L,Bl}$ = 0.52%, when unloaded $\xi_{L,Bu}$ = 0.39%; for the specimen CFRP-C, when loaded $\xi_{L,Cl}$ = 0.51%, when unloaded $\xi_{L,Cu}$ = 0.52%.

4.4 Repeatability

Repeatability refers to the sensor's ability to provide consistent center wavelength readings under constant working conditions. This is determined by performing repeated full-scale tests in a single direction and calculating the deviation across the resulting data sets. The repeatability error of the sensor is used to reflect the performance index of repeated loading and unloading under full-range conditions, and whether the central wavelength can be repeated and consistent. It can be calculated according to Eq. (32):

$$\xi_R = \frac{\Delta\lambda_{R,\max}}{(\Delta\lambda)_{FS}} \times 100\% \tag{32}$$

where $\Delta\lambda_{R,\max}$ is the maximum deviation of the center wavelength of the loading and unloading grating during the calibration test, and $(\Delta\lambda)_{FS}$ is the variation of the center wavelength value of the full-scale grating.

According to the calibration test data in Fig. 9, the maximum deviation value of the center wavelength of each grating can be obtained: for the specimen CFRP-A, it is 0.2373 nm when loaded and 0.2546 nm when unloaded; for the specimen CFRP-B, the loading is 0.2041 nm, and the unloading is 0.2038 nm; for the specimen CFRP-C, it is 0.3144 nm when loaded and 0.4082 nm when unloaded.

Based on Eq. (32), the repeatability error of each specimen can be calculated as follows: for the specimen CFRP-A, $\xi_{R,Al}$ = 1.65% when loading and $\xi_{R,Au}$ = 1.77% when unloading; for the specimen CFRP-B, $\xi_{R,Bl}$ = 1.40% when loading, and $\xi_{R,Bu}$ = 1.40% when unloading; for the specimen CFRP-C, $\xi_{R,Cl}$ = 2.17% when loading, and $\xi_{R,Cu}$ = 2.82% when unloading.

4.5 Total Accuracy

To evaluate the overall reliability of FBG sensors in the intelligent CFRP plates, it is usually expressed in total accuracy. The total accuracy indicates that in the actual application process, the actual center wavelength value of the grating is within a range of its theoretical characteristics or working characteristics under a certain confidence probability, which can be calculated according to Eq. (33):

$$\xi_P = \sqrt{\xi_H^2 + \xi_L^2 + \xi_R^2} \tag{33}$$

After substituting the linearity, hysteresis and repeatability indexes of the three intelligent CFRP plate gratings calculated above into Eq. (32), the total accuracy of each grating can be mastered, and then all the indexes are summarized to form Table 8.

Comprehensively considering the indicators in Table 8, the FBG in intelligent CFRP plate has excellent sensing performance and can effectively monitor the stress characteristics and strain of the CFRP plate.

Table 8: Summary of calibration results of three intelligent CFRP plate gratings.

Specimen	Measurement Solutions	Hysteresis	Linearity	Repeatability	Total Accuracy
CFRP-A	Load	0.94%	0.57%	1.65%	1.98%
	Unload		0.38%	1.77%	2.04%
CFRP-B	Load	0.90%	0.52%	1.40%	1.74%
	Unload		0.39%	1.40%	1.71%
CFRP-C	Load	0.68%	0.51%	2.17%	2.33%
	Unload		0.52%	2.82%	2.95%

4.6 Statistical Variability and Uncertainty

Only three CFRP plates were tested in this study, which inevitably limits the statistical robustness of the results. Nevertheless, simple statistical descriptors can still provide useful information on the expected variability of the main performance indices. For each key parameter (strain sensitivity, hysteresis, linearity, repeatability, and total accuracy), the mean value, sample standard deviation, coefficient of variation (CV), and an approximate 95% confidence interval (CI) for the mean were calculated using the data in Tables 1–4 and 8.

For hysteresis, the three specimens give values of 0.94%, 0.90%, and 0.68%, yielding a mean of about 0.84% with a standard deviation of 0.14% and a CV of approximately 17%. Assuming an underlying normal distribution at the specimen level, the corresponding 95% CI for the mean hysteresis error is roughly 0.5%–1.2%. For linearity, the values of 0.57%, 0.52%, and 0.51% lead to a mean of about 0.53%, a standard deviation of 0.03%, and a CV of about 6%, with an approximate 95% CI of 0.45%–0.61%.

When both loading and unloading cases are considered (six values in total), the repeatability error has a mean value of approximately 1.87% and a standard deviation of about 0.55%, corresponding to a CV of about 29%. The associated 95% CI for the mean repeatability error is therefore about 1.3%–2.4%, which is consistent with the spread of the individual repeatability values (1.40%–2.82%). Similarly, the total accuracy values have a mean of about 2.13% with a standard deviation of roughly 0.46% (CV ≈ 22%), giving an approximate 95% CI for the mean total accuracy of 1.6%–2.6%. Strain sensitivity exhibits only very small scatter, with a CV well below 1%, indicating that the basic wavelength–strain calibration is highly stable across specimens.

Taken together, these statistics show that, while noticeable scatter exists—particularly in repeatability and, consequently, in total accuracy—the variability remains moderate and acceptable for practical SHM applications. Reporting the standard deviation, CV, and approximate confidence bounds for these metrics provides readers with a clearer quantitative picture of the expected accuracy and uncertainty when smart CFRP plates of the same type are fabricated and deployed in practice. However, because of the limited number of specimens, these estimates are not fully representative, and a larger test series would be required for more robust reliability and uncertainty assessment.

5 Conclusions

In this paper, three smart CFRP plates were calibrated and tensioned in accordance with the national standard. The sensing performance of the intelligent CFRP plate was evaluated in terms of strain sensitivity, hysteresis, linearity and repeatability. The following conclusions are drawn.

(1) By considering the strain transfer among the fiber core, coating, adhesive layer, and CFRP substrate, the average strain-transfer coefficient along the grating length was derived as shown in Eq. (34).

$$\alpha\left(k, L_f\right) = 1 - \frac{sh\left(kL_f\right)}{kL_f ch\left(kL\right)} \tag{34}$$

Based on this model, the structural parameters were optimized, resulting in a groove depth and width of 0.5 mm × 0.5 mm, an adhesive thickness of 0.4 mm, and a bonding length of 40 mm for the FBG sensor. Under the present configuration, the average strain-transfer coefficient is close to unity ($\alpha > 0.99$), so the strain-transfer correction is negligible in engineering practice.

(2) According to the calculation method of the static performance index in the national standard, the strain sensitivity of the FBG was determined. The test results show that the strain sensitivity is no less than 1.21 pm/με, which is close to the theoretical value thereby verifying the feasibility of the design structure, so as to provide support for the subsequent determination of the stability of the FBG sensor.

(3) The results of loading and unloading tests on intelligent CFRP plates and linear fitting of the collected data show that the hysteresis of the embedded strain sensor of the intelligent CFRP plate is no more than 0.94%, linearity is no bigger than 0.57%, repeatability is no higher than 2.82% and total accuracy is no larger than 2.95%, which can indicate that the good sensing ability of intelligent CFRP plate and meets the needs of the actual project.

(4) By pre-tensioning the CFRP plate to 0.3Pc and then pasting the FBG, the results of tension test show that the monitoring strain can reach 12088.71 με, and 90% of the nominal ultimate bearing capacity of CFRP plate can be monitored. Therefore, the CFRP plate employing the designed structure coupled with fiber grating may fully and effectively monitor the stress and strain condition of the CFRP plate during usage, and better ensure the safety and reliability of the reinforced structure.

(5) From a practical SHM standpoint, embedding a large-range FBG in a prestressed CFRP plate yields a compact, self-sensing strengthening system that is well protected from the environment and simple to install on site. Such a device can track both service-level and pre-failure strains over the full life cycle of real bridge structures. To confirm and quantify long-term durability, future studies will include accelerated environmental-exposure tests, cyclic fatigue loading, and full-scale validation on in-service bridges, together with further optimisation of the encapsulation process and prestress level to enhance fatigue life and sensor survival.

Acknowledgement: None.

Funding Statement: This work was supported by the Guangxi Science and Technology Base and Talent Special Program (Guike AD25069013) and by the Guangxi Natural Science Foundation (Grant No. 2025GXNSFAA069403).

Author Contributions: Mingxia Li conceived and designed the study, developed the theoretical model, led the experiments and data collection, performed validation and visualization and drafted the manuscript. Haowei Xu assisted with experiments, contributed to theoretical derivations, data curation and formal analysis, supported the theoretical interpretation and assisted with manuscript drafting and completion. Ruiqi Li contributed to theoretical derivations and numerical implementation, prepared figures and tables and performed consistency checks. Bo Song provided engineering resources, participated in specimen fabrication and instrumentation, coordinated the test setup and execution, conducted data acquisition and contributed to manuscript revision. Wanxu Zhu supervised the project and provided resources, offered methodological guidance, refined the manuscript, secured funding and approved the final version. All authors reviewed and approved the final version of the manuscript.

Availability of Data and Materials: The authors confirm that the data supporting the results of this study are available in the article.

Ethics Approval: Not applicable.

Conflicts of Interest: The authors declare no conflicts of interest.

References

1. Czaderski C, Motavalli M. 40-year-old full-scale concrete bridge girder strengthened with prestressed CFRP plates anchored using gradient method. Compos Part B Eng. 2007;38(7–8):878–86. doi:10.1016/j.compositesb.2006.11.003.
2. You YC, Choi KS, Kim J. An experimental investigation on flexural behavior of reinforced concrete beams strengthened with prestressed CFRP sheets. Compos Part B Eng. 2012;43(8):3026–36. doi:10.1016/j.compositesb.2012.05.030.
3. Michels J, Martinelli E, Czaderski C, Motavalli M. Prestressed CFRP strips with gradient anchorage for structural concrete retrofitting: experiments and numerical modeling. Polymers. 2014;6(1):114–31. doi:10.3390/polym6010114.
4. Piątek B, Siwowski T. Experimental study on flexural behaviour of reinforced concrete beams strengthened with passive and active CFRP strips using a novel anchorage system. Arch Civ Mech Eng. 2022;22(1):45. doi:10.1007/s43452-021-00364-7.
5. Chan THT, Yu L, Tam HY, Ni YQ, Liu SY, Chung WH, et al. Fiber Bragg grating sensors for structural health monitoring of Tsing Ma bridge: background and experimental observation. Eng Struct. 2006;28(5):648–59. doi:10.1016/j.engstruct.2005.09.018.
6. Jayawickrema UMN, Herath HMCM, Hettiarachchi NK, Sooriyaarachchi HP, Epaarachchi JA. Fibre-optic sensor and deep learning-based structural health monitoring systems for civil structures: a review. Measurement. 2022;199(3):111543. doi:10.1016/j.measurement.2022.111543.
7. Gallego JM, Czaderski C, Michels J. Prestress force-release tests at elevated temperatures—gradient anchorage stability for prestressed EB CFRP strips. Compos Struct. 2016;137(1):159–69. doi:10.1016/j.compstruct.2015.11.022.
8. Yang M, Xu H. Application of fiber Bragg grating sensing technology and physical model in bridge detection. Results Phys. 2023;54(1):107058. doi:10.1016/j.rinp.2023.107058.
9. Bado MF, Casas JR. A review of recent distributed optical fiber sensors applications for civil engineering structural health monitoring. Sensors. 2021;21(5):1818. doi:10.3390/s21051818.
10. Zhou H, Wang Y, Zhou Z, Ma C. Effects of bonding on Fiber Bragg Grating (FBG) sensor for monitoring steel corrosion condition in concretes. Measurement. 2023;222:113565. doi:10.1016/j.measurement.2023.113565.
11. Subramaniam KVL, Ghosn M, Ali-Ahmad M. Influence of variation in the local interface fracture properties on shear debonding of CFRP composite from concrete. J Adhes Sci Technol. 2017;31(19–20):2202–18. doi:10.1080/01694243.2016.1261505.
12. Abu Hassan MR, Abu Bakar MH, Dambul K, Adikan FRM. Optical-based sensors for monitoring corrosion of reinforcement rebar via an etched cladding Bragg grating. Sensors. 2012;12(11):15820–6. doi:10.3390/s121115820.
13. Cheng Y, Zhao C, Zhang J. A two-level strategy to assess the bearing capacity of corroded structures via long-gauge fiber-optic sensors. Structures. 2023;56(4):104970. doi:10.1016/j.istruc.2023.104970.
14. Abedin S, Biondi AM, Wu R, Cao L, Wang X. Structural health monitoring using a new type of distributed fiber optic smart textiles in combination with optical frequency domain reflectometry (OFDR): taking a pedestrian bridge as case study. Sensors. 2023;23(3):1591. doi:10.3390/s23031591.
15. Li W, Chen S, Chu Y, Huang P, Yan G. Wide-range fiber Bragg grating strain sensor for load testing of aircraft landing gears. Optik. 2022;262(25):169290. doi:10.1016/j.ijleo.2022.169290.
16. Feng DQ, Luo XD, Fan W, Zhu BH, Qiao XG. Strain sensing performance of material packaged fiber Bragg grating in wide temperature range. Acta Opt Sin. 2021;41(21):2106004. (In Chinese).
17. Sanchez MRA, Leal-Junior AG, Segatto MV, Marques C, Dos Santos WM, Siqueira AAG, et al. Fiber Bragg grating-based sensor for torque and angle measurement in a series elastic actuator's spring. Appl Opt. 2018;57(27):7883–90. doi:10.1364/AO.57.007883.

18. Kuang Y, Guo Y, Xiong L, Liu W. Packaging and temperature compensation of fiber Bragg grating for strain sensing: a survey. Photonic Sens. 2018;8(4):320–31. doi:10.1007/s13320-018-0504-y.
19. Zhou Z, Wang Z. An experimental investigation on flexural behavior of reinforced concrete beams strengthened by an intelligent CFRP plate with built-In optical fiber Bragg grating sensors. J Sens. 2018;2018(1):4271751. doi:10.1155/2018/4271751.
20. Ye Y, Hu S, Fan X, Lu J. Effect of adhesive failure on measurement of concrete cracks using fiber Bragg grating sensors. Opt Fiber Technol. 2022;71(6):102934. doi:10.1016/j.yofte.2022.102934.
21. Butov OV, Przhiialkovskii DV, Lopunov AI, Pnev AB. Strength properties of femtosecond-induced defects and weak Bragg gratings for distributed optical fiber sensors. Opt Laser Technol. 2023;162:109271. doi:10.1016/j.optlastec.2023.109271.
22. Wang G, Wang J, Meng J, Ren L, Fu X. Design, calibration, and application of a wide-range fiber Bragg grating strain sensor. Sensors. 2025;25(4):1192. doi:10.3390/s25041192.
23. Falcetelli F, Rossi L, Di Sante R, Bolognini G. Strain transfer in surface-bonded optical fiber sensors. Sensors. 2020;20(11):3100. doi:10.3390/s20113100.
24. Liu Z, Liu X, Zhu SP, Zhu P, Liu W, Correia JAFO, et al. Reliability assessment of measurement accuracy for FBG sensors used in structural tests of the wind turbine blades based on strain transfer laws. Eng Fail Anal. 2020;112(2):104506. doi:10.1016/j.engfailanal.2020.104506.
25. Perry M, Yan Z, Sun Z, Zhang L, Niewczas P, Johnston M. High stress monitoring of prestressing tendons in nuclear concrete vessels using fibre-optic sensors. Nucl Eng Des. 2014;268:35–40. doi:10.1016/j.nucengdes.2013.12.038.
26. Wang C, Cheng L. Use of fiber Bragg grating sensors for monitoring concrete structures with prestressed near-surface mounted carbon fiber-reinforced polymer strips. J Intell Mater Syst Struct. 2014;25(2):164–73. doi:10.1177/1045389x13489364.
27. Kerrouche A, Boyle WJO, Sun T, Grattan KTV, Schmidt JW, Taljsten B. Strain measurement using embedded fiber Bragg grating sensors inside an anchored carbon fiber polymer reinforcement prestressing rod for structural monitoring. IEEE Sens J. 2009;9(11):1456–61. doi:10.1109/JSEN.2009.2018355.
28. Liu FR, Zhu WX, Zeng ZY, Chen HJ, Gao C. Design and test of prestressed carbon fiber plate coupling long range fiber grating. Build Technol Dev. 2020;47(11):22–4. (In Chinese).
29. Zeng ZY, Zhu WX, Liu FR, Wei W, Li MG, Li MX. Research on sensing characteristics of CFRP plates coupled with large-range fiber gratings. Ind Constr. 2020;50(9):174–80. (In Chinese). doi:10.13204/j.gyjzG20010406.